RSC Advances

ROYAL SOCIETY OF CHEMISTRY

www.rsc.org/advances

Structural and electronic properties of tungsten nanoclusters by DFT and basin-hopping calculations

Ken-Huang Lin[1], Shi-Liang Wang[2], Chuan Chen[3], and Shin-Pon Ju[1,*]

[1]Department of Mechanical and Electro-Mechanical Engineering, National Sun-Yat-Sen University, Kaohsiung, 804, Taiwan

[2]School of Physics and electronics, Central South University, Changsha, 410083, China

[3]Department of Information Management, Meiho Institute of Technology, Pingtung 912, Taiwan

*Corresponding authors (jushin-pon@mail.nsysu.edu.tw)

Abstract: The structural and electronic properties of small tungsten nanoclusters W_n (n=2-16) were investigated by density functional theory (DFT) calculations. For the W nanocluster, the lowest-energy structures were first obtained by basin-hopping method (BH) with thetight-binding many-body potential for a bulk tungsten material. These structures were further optimized by the DFT calculation in order to find better parameters of the tight-binding (TB) and Finnis-Sinclair (FS) potential appropriate for W nanocluster s. The values of binding energy and second-order energy difference reveal that the structure W_{11} has a relatively higher stability than those of other sizes. The vertical ionization potential (VIP), adiabatic electron affinity (AEA) and HOMO-LUMO gap are also discussed for W nanocluster s of different sizes. In addition, large size nanoclusters W_n(n=30-120) are obtained by BH method, and a comparison of the structural properties determined by TB and FS potentials are represented with Honeycutt–Andersen index analysis.

Keywords: Density functional theory, tight-binding potential, basin-hopping, tungsten nanocluster, HA index.

1. INTRODUCTION

The refractory metal tungsten (W) has excellent physical and chemical properties, such as high melting point (about 3420 ^{o}C), high density (19.3 g/cm^3), high strength and excellent creep resistance at room and elevated temperature, high electron emissivity and low vapor pressure[1]. The applications of W have now covered quite various fields such as lighting, electronics, catalysis, high-temperature technology, medicine, aviation, military uses, and so on[2-4]. W nanostructures, due to their large surface-volume ratio, quantum size effects and surface effects exhibit some different thermal, mechanical, electronic and chemical properties when compared to the bulk counterpart, and thus exhibit high potential applications as nano-interconnectors, high-performance catalysts, nano-electron-emitters. In the last few decades,W nanoclusters with diameters of 10 - 100 nm have been produced by several methods[5] , such as salt assisted combustion reaction (SACR)[6], plasma processing technique (PPT)[7], electrical explosion of wires[8], high energy ball-milling[9], and physical vapor deposition (PVD)[10]. Moreover, W nanocluster with size below 10 nm, called nanoclusters later, have also been synthesized by the different methods of molten salt–assisted self-propagating high-temperature synthesis (SHS)[11], metal-doped[12], gas-phase combustion synthesis[13], solvothermal decomposition method[14], and other chemical reduction process[15,16]. However, due to some technical problems in experiments, it is quite difficult to confirm their structures and electronic properties.

It has been well-demonstrated that theoretical calculations and simulations are an powerful alternative to the direct experiments for investigating the nanoclusters, and have been widely applied to explain and/or forecast the size-dependent properties. The structures and electronic properties of W_n (n=2, 3) clusters have been studied using density functional theory (DFT) calculation by Wu *et al.*[17]. Their results have also been compared with those of experiment [18]. Furthermore, Zhang *et al.*[19] investigated the geometry and electronic structures of anionic and neutral states of W_n (n=2-4) clusters. They found out the stable geometry for each size cluster, and then analyzed the frequency results, binding energy and photoelectron spectra (PES) of clusters[20]. Zhang's group[21] also investigated the adsorption properties of N_2 molecules on neutral, anionic, and cationic W_n (n=2-5) clusters using DFT at B3LYP and PW91 levels. They found by electronic and frequency analysis[19,22] that the bond length and frequency influences the adsorptive ability between the W cluster and N_2 molecule[23-25].

Since structural change is always an important factor influencing the catalytic and electronic properties of material, this study performs DFT calculations to investigate the structural and electronic properties of W_n (n=2-16) nanoclusters. To understand the electronic structures of tungsten nanoclusters, the stable geometry of W_n(n=2-16) nanoclusters [26] must also be found. Therefore, we first employ the molecular static (MS) of big-bang (BB) and basin-hopping (BH) algorithms to find the most stable configuration of W_n (n=2-16) nanoclusters. In order to obtain more accurate structures, the Dmol^3 quantum chemical package was used to optimize these product configurations found in MS simulation. The detailed procedures of the lowest-energy structure search are introduced in the simulation model section. Finally, the binding energy, second-order energy difference, HOMO-LUMO gap, ionization potential and electronic affinity of tungsten nanoclusters W_n (n=2-16) were investigated by DFT calculations.

2. SIMULATION MODEL

2.1 Small W_n (n=2-16) nanoclusters modeled by DFT

The size effect on the structural stability and electronic properties of the W nanoclusters was investigated by DFT. Above all, the most important procedure is to first obtain the energetically favorable configuration of the tungsten nanocluster, i.e., the lowest-energy structures of W nanoclusters (global minima structures), before determining the nanocluster properties. For this purpose, two stochastic methods, i.e., the big bang (BB)[27, 28] and basin-hopping (BH)[29,30] algorithms, were first carried out by using tight-binding [31,32] and Finnis Sinclair (FS) potential[33]. In the traditional BH method, a conjugate gradient method was used to reach the local minimum where a new geometry is generated. In our BH method, the conjugate gradient method was replaced by the limited memory BFGS method (LBFGS) [34], which can be used to simulate a system consisting of a great number of atoms and whose calculation rate in the BH method is faster than that of the conjugate gradient method.

The interaction between two W atoms depends not only on the distance between those atoms, but also on their local environment. The algorithm for computing this potential is relatively simple compared to other many body potentials. This model commences by summing the band energy, which is characterized by the second moment of the d-band density of state (DOS), and a pairwise potential energy of the Born–Mayer type. The TB interatomic energy of atom *i* is thus expressed as follows[31]:

$$E_i = -\left\{ \sum_j \xi^2 \exp\left[-2q\left(r_{ij}/r_0 - 1\right)\right] \right\}^{1/2} + \sum_j A \exp\left\{-p\left(r_{ij}/r_0 - 1\right)\right\} \quad (1)$$

where ξ is an effective hopping integral, r_{ij} is the distance between atom *i* and *j*, and r_0 is the first-neighbor distance. The parameters A, p, q, and ξ for bulk W material are listed in Table 1[35]. In addition, the FS potential are also used to find the initial structures of W nanocluster. The potential fomular is given by:

$$U_{FS} = U_N + U_P = \frac{1}{2}\sum_{ij} V\left(r_{ij}\right) - A\sum_i \sqrt{\rho_i} \quad (2)$$

where the U_N and U_{Np}stand for N-body and repulsive terms, respectively. The r_{ij} is the inter atomic distance between atom *i* and *j*. The density is given by$\rho\left(r_{ij}\right) = \sum_{j\neq i} \phi(r_{ij})$, and the density function ϕ and cut-off distance are described as follows:

$$\phi\left(r_{ij}\right) = \begin{cases} (r_{ij} - d)^2 r_{ij} \le d \\ 0 \qquad\qquad r_{ij} > d \end{cases} \quad (3)$$

where the parameter *d* are set depend on lattice constant. Further, the repulsive part is given by:

$$V\left(r_{ij}\right) = \begin{cases} \left(r_{ij} - d\right)^2 (c_0 + c_1 r_{ij} + c_2 r_{ij}^2) & r_{ij} \le c \\ 0 & r_{ij} > c \end{cases} \quad (4)$$

where the parameter of c_0, c_1, and c_2 are the fitting parameters, $c$is a cut-off parameter assumed to lie between the second and the third neighbor atoms.

To find the globe minima structure, one hundred lowest-energy structures for each W_n (n=2-16) nanocluster, obtained by BB and BH method with TB potential and FS potential. Furthermore, these structures were optimized by DMol^3 package[36, 37] with DFT simulation in order to

determine more accurate structures. The DMol[3] package sets employed density functional Semi-core PseudoPotentials (DSPP) calculations with double numerical basis sets polarization *p*-functional (DNP), and the generalized approximation (GGA)[38] by Perdew and Wang parameterization (PW91)[39,40] correction. Spin-polarization was considered in our calculation. The self-consistent field (SCF) tolerance and integration accuracy were all set to "fine" with high accuracy of 10^{-6} au for energy convergence. After the W clusters from BB and BH methods were fully optimized by means of the DMol[3] package to obtain the three lowest-energy structures of W_n(n=2-16).

2.2 Large W_n (n=30-120) nanoclusters modeled by the Honeycutt–Andersen (HA) index

Large tungsten nanoclusters were also considered in this simulation, with the FS and TB potentials applied to analyze the structural properties. A useful assessment of local configuration is given by the method of Honeycutt-Andersen (HA) index analysis[41]. The sequence of four integers (*i,j,k,l*) and the concept of radial distribution function (RDF) for finding the near-neighbor atoms are employed to define the different configuration distribution of local structures. The first integer of this index is useful in judging whether or not the root pair of two random atoms is bonded; it is 1 when bonding exists, 2 if not. The second integer represents the number of near-neighbor atoms shared in common by the root pair; the third integer stands for the number of near-neighbor bonds between the shared neighbors; the fourth integer is used to distinguish different structures which share the same preceding three numbers. According the HA index analysis, body centered cubic (BCC) structures are described by 1441, and face centered cubic (FCC) by 1421. In addition, the index 1422 consists of 50% FCC and 50% hexagonal close packed (HCP) structures.

3. RESULTS AND DISCUSSION

3.1 Small W_n (n=2-16) nanocluster and DFT calculation

To verify the reliability of our DFT model, Table 2 lists the calculated lattice constant and cohesive energy compared with experimental values of tungsten BCC, FCC, and HCP lattices[42, 43]. The binding energy by BPW91 correction in previous study is also presented[44]. We calculate the properties of W bulk material by BPW91 and PW91, but the binding is closer to the bulk when using the PW91function. Moreover, the lattice constant is 3.165 nm, also in near agreement with the experiment values of 3.16 nm and 3.25 nm[45, 46]. We employ the two functional of PW91 and BPW91 to calculate the bond length, frequency, and dissociation energy of the tungsten dimer cluster, shown in Table 3, with calculation setups of **PW91/DNP/DSPP** and **BPW91/DNP/DSPP.** Also shown are results of previous studies, both experimental and theoretical. The bond length results are different by changing initial bond length, and the frequency and dissociation energy of ω = 249.7 and 387.5 cm^{-1} and E_d= 5.34 and 5.49 eV are very close to the experimental values[47, 48]. According to this preliminary test calculation on the W dimer by using different functional methods, **PW91/DNP/DSPP** appears more accurate, and is used to study the remaining cases.

After optimized by DFT, three lowest-energy isomers for each W nanocluster are presented in Figure 1. The energy of the lowest-energy isomer was used as the reference value for the W nanoclusters of the same size. The values in the parentheses are energy differences between the

isomers and the lowest-energy structure. The binding energies and average bond lengths of the lowest-energy W_n(n=2-16) nanoclusters were calculated to understand the stability and structural properties of W nanoclusters, these results are listed in Table 4. The binding energy per atom E_b can be determined by the following equation:

$$E_b=[E_{Tol} - n\times E_{atom}]/n \quad (5)$$

where E_{Tol} is the total electronic energy of the W nanocluster with atom number n, and E_{atom} is the electronic energy of an isolated W atom. In Figure 2, the binding energy of the W nanocluster increases with the enhancement of the nanocluster size, demonstrating that a larger nanocluster will have higher thermal stability. This can be attributed to the fact that the average bond lengths of W atoms will increase for a larger W nanocluster, which leads to the significant overlap of *6p* orbital and the increase in the binding energy. For n= 3 to 8, the binding energy of 2D ground-state nanocluster (2D structures are shown in Supporting Information) displays a sharp increase from 3.74 to 4.65 eV, while for n = 2 to 16, the binding energy of 3D ground-state nanocluster shows a relatively slight increase from 2.67 to 6.03 eV. The binding energy of the largest W nanocluster, W_{16}, has reached 68% of the binding energy of bulk W material. The variation of average bond length seems to be sensitive to the nanocluster with average W-W bond lengths for n=2 to 16 being between 2.65 and 2.61Å, about 10-14% shorter than that in bulk W material[49].

The second-order energy difference (Δ_2E) is also discussed in the present study because it is a useful parameter to examine the relative stability of the W_n nanocluster with respect to W_{n+1} and W_{n-1}. This parameter is defined as Eq. (6)[50].

$$\Delta_2E(W_n)=[E(W_{n-1})+E(W_{n+1})-2E(W_n)] \quad (6)$$

where E (W_n)is the total energy of W nanocluster with n atoms. Figure 3 shows the profile of Δ_2E (W_n) as a function of the atom number n. For n=11, a peak with a positive Δ_2E value indicates that the W_{11} displays relatively higher thermal stability than W_{10} and W_{12}. The energy of the first isomer of W_{11} is found to be the closest to the ground-state and all energy differences are smaller than 1 eV. For the ground-state geometry of W_{12}, it is capped pentagon bipyramidal[51-53]. Note that the ground-state geometry of W_{13} is not perfectly icosahedral, unlike previous configurations found for W_{13}. It can be seen that a surface atom sticks slightly out from the cluster surface in Figure 1. In fact, we also can obtain by using BB and BH method with tight-binding potential parameters. However, the geometry of C1 symmetry is more stable configuration after DFT optimization in our calculation progress.

Figure 4 shows the profile of HOMO-LUMO gap[50, 54]for the W nanocluster with different sizes. It can be found that almost gaps of W_n (n=2-16) were larger than 0.15 eV. W_2, W_3, and W_4 have larger gaps than 0.5 eV, indicating the higher chemical inertness of these nanoclusters. A drop in the HOMO-LUMO gap was found when the size of W nanocluster becomes larger than 5. These significant orbital overlaps also cause a considerable increase in the binding energy when the size is larger than 5, and the slop of binding energy curve are gradually smooth as shown in Figure 2. This result reflects the fact that more atomic orbitals overlap and the energy levels become gradually closer for a larger W nanocluster. Furthermore, the profile of the HOMO-LUMO gap presents a general odd-even oscillation, where the gap of nanoclusters with odd-numbered atoms is larger than neighboring even-numbered ones.

In order to investigate the electron donating and accepting ability of W nanoclusters with different sizes, both vertical ionization potential (VIP) and adiabatic electron affinity (AEA)[53,55] were calculated. The VIP is defined as the minimum required energy to remove an electron from the W nanocluster at the ground state, a value that can be determined by the energy difference between the neutral and cation species with the same geometry at the ground state. The VIP value can be represented by the following relation:

$$VIP=W(E^{+})-W_{opt}(E^{0}) \quad (7)$$

where $W(E^{+})$ and $W_{opt}(E0)$ are the electronic energies of the cation and neutral nanoclusters with the same geometry at the ground state, respectively. The VIP profile as a function of W atom number is shown in Figure 5. The variation of VIP value with the W atom number is insignificant and varies near 5 eV.

The AEA is defined as the energy change after the W nanocluster attains an electron. This parameter can be estimated by the energy change between the neutral and the anion W nanoclusters with the same geometries at the ground state. The AEA of the W nanoclusters are calculated by the following relationship,

$$AEA=W_{opt}(E^{0})-W(E^{-}) \quad (8)$$

where $W(E^{-})$ is the energy of anion nanocluster. If AEA is positive, the anion nanocluster is more stable than the neutral one. The AEA profile as a function of W atom number is shown in Figure 6, suggesting that The AEA values of W_n (n=2-16) were all positive. The AEA value dramatically increases with the increase in W nanocluster size, implying that a electronic transfer of chemical reaction from the adsorbed molecule to W nanocluster is more preferable for large size nanocluster.

It is well-known that the distribution of valence electrons of a W atom is located in the *s* and *d* orbital, which is filled in $5d^4 6s^2$. When W atoms gather together as a cluster, their itinerant electrons are affected by the interaction between W atoms and may lead to the excitation of itinerant electrons to the higher energy level orbital (i.e., 6*p* orbital), causing an electronic disturbance in the valence-band. Therefore, the Mulliken population analysis of W_n (n=2-16) nanoclusters was calculated to investigate the valence electronic structures listed and showed in Table 5 and Figure 7 for the electronic charges in 5d, 6s, 6p and the sum. The charge is between 4.44 and 4.56 in the *5d* orbital and 1.17 to 1.5 in the 6s orbital. From Table 5, it can be observed that the charge distribution for all cases have partially filled the 5*d*, 6*s* and 6*p* orbitals. However, most of the valence electrons are located in the 5*d* and 6*s* orbitals. The charge distribution of n = 15 and 16 shows a larger electronic transfer in 6*s* compared to other nanoclusters. This result may explain why their AEAs have the lowest value. In addition, the electronic distribution of the 6*p* orbital for small size nanoclusters is lower than that for other nanoclusters. This is probably caused of the higher band gap energy.

3.2 Large W_n (n = 30-120) nanoclusters and HA index analysis

Large nanoclusters are also considered by the progress of searching global minima structures. Previous studies have indicated that the TB potential is most suitable to describe FCC and HCP structures[31], and FS is preferable for BCC configurations. However, until now, the studies of W nanoclusters which use the FS potential are still lack. We employ both TB and FS potentials to find

the lowest-energy structures by BH method. The HA index analysis is represented in Figure 8.The red, pink, green, and orange lines represent the fractions of BCC, FCC, FCC-HCP phases, and amorphous structures, respectively. There are different phase transitions which can be observed in three regions. At sizes smaller than 45 atoms, the crystal phases are not ordered significantly. At sizes larger than W_{45}, the fraction of 1422 HA index increases significantly. At sizes larger than about 80 atoms, the fraction of 1421 and 1422 HA index configurations rise with a concomitant drop in amorphous levels. Moreover, the fraction of BCC phase does not follow any specific tendency while size increases. In addition, the lowest-energy structures for large size nanoclusters found using FS potentials are represented in Figure 9. Clearly, the fraction of BCC phase is higher than other crystal types for nanoclusters ranging from sizes of 30 to 120. It can be observe that the lowest-energy structures at the size of 60, and 116 possess higher properties of BCC pahse, these structures are shown in Figure 10 (a)-(d). The cubic structures are easily associated with BCC crystal for W_{60}, as shown in panel (a). However, It is not similar to the structure which found by TB potential in Figure 10 (b). In the case of W_{116} , FS-used structure also represents a higher fraction of BCC phase than TB-used strcuture , as shown in Figure 10 (c) and (d). In the FS-used abd TB-used structure distribution, the 1422 HA index peak can be observed at the 54-56 atom range. The lowest-energy structures of W_{54} are found by both the FS and TB potentials are the same, as shown in Figure11(a). We analyze the structure of W_{54} by HA index, the amorphous structures can also be calculated and excluded for reveal the configuration of different phases. In general, the amorphous phase fraction is higher in the large nanoclusters because the surface atoms are also calculated when all atoms are considered in the HA index analysis. In Figure 11(b), the pair fractions are shown, all the pairs of atoms which are included in the crystal structures in W_{54} nanoclusters. The yellow atoms are the *i* atom and *j* atom which are the basic pair; the standard 1422 arrangement is shown by the blue atoms, and the other green atoms are neighbor atoms of the i-j pair in calculations. From W_{54}, the different results between FS and TB are rising depend on the increase of size (The other sizes of W nanoclusters are shown in Supporting Information).

3. CONCLUSIONS

We use DFT method to investigate the structural and electronic properties of small tungsten nanoclusters W_n (n=2-16). The global minima structures using the TB and FS potential for W nanoclusters are found. The geometry of W_n (n=2-16) nanoclusters with stable energy are determined by using (BB) and basin-hopping (BH) methods. The DMol^3 package is employed to find the configuration of nanoclusters with lowest energy. The results of calculating binding energy demonstrate that W_{11} has the highest stability. The average bond length seems to be insensitive to the nanoclusters size for W_n (n=2-16), but are shorter than that in bulk W material. In addition, a peak with a positive $\Delta_2 E$ value indicates that the nanocluster for n=11 is more stable than nanoclusters close in size. Furthermore, the n=2 and 14 nanoclusters are found have the highest and lowest VIP values, respectively. Our AEA results show that W_n (n=2-16) are all positive and the value rises with increasing nanocluster size. According to these AEA results, W_{15} has better properties for electronic transfer. In the large size nanoclusters study, W_n (n=30-120) nanoclusters were found by TB and FS

potential. The higher fraction of BCC phase is represented when the FS potential was used, and high fractions of FCC and HCP phase are shown when we employed TB potential. Interesting, both TB and FS potential are used in the size of W_{54} nanocluster, the same structure are found. This structure are considered to a special size which posses a significant fraction of HCP phase. From the HA index analysis, the FS potential indeed reflect the cubic structures of W materials than TB potential. In this study, we conclude that the W nanoclusters are not must BCC or FCC and HCP configurations in small size. Beacuse it need to spend too many computation time on the DFT calculation of large W nanoclusters. The larger tungsten clusters will be topics of future study.

Acknowledgements:

The authors would like to acknowledge the (1) National Science Council, Republic of China, under Grant Number NSC 101-2628-E-110-003-MY3 for the financial support, (2) National Center for High-performance Computing, Taiwan, for the use of computer time, (3) National Center for Theoretical Sciences, Taiwan.

References

1.Lassner E.,Schubert W.D., Tungsten: Properties, Chemistry, Technology of the Element, Alloys, and Chemical Compounds. **1998**, New York.

2. Wallace, W. T.; Whetten, R. L. *J. Am. Chem. Soc.* **2002**, *124*, 7499−7505.

3. Kim, H. Y.; Kim, D. H.; Ryu, J. H.; Lee, H. M. *J. Phys. Chem. C.* **2009**, *113*, 15559−15564.

4. Gustafson, J.; Westerstrom, R.; Balmes, O.; Resta, A.; van Rijn, R.; Torrelles, X.; Herbschleb, C. T.; Frenken, J. W. M.; Lundgren, E. *J. Phys. Chem. C.* **201**0, *11*4, 4580−4583.

5.Henry H. Hwu, Brian D. Polizzotti, Jingguang G. Chen. *J. Phys. Chem. B* **2001,** *105,* 10045-10053

6.Benziger, J. B.; Ko, E. I.; Madix, R. J. *J. Catal.* **1978**, *54*, 514.

7.Friend, C. M.; Stevens, P. A.; Serafin, J. G.; Baldwin, E. K.; Madix, R. J. *J. Chem. Phys.* **1987**, *87*, 1847.

8.Stevens, P. A.; Friend, C. M.; Madix, R. J. *Surf. Sci.* **1988**, *205*,187.

9.Fruhberger, B.; Chen, J. G. *J. Am. Chem. Soc.* **1996**, *118*, 11599.

10. Fruhberger, B.; Chen, J. G. *Surf. Sci.* **1995**, *38*, 342.

11. H.H. Nersisyan, J.H. Lee, and C.W. Won. C*ombust. Flame* **2005**, *142*, 241.

12. R.K. Barik, A. Bera, A.K. Tanwar, I.K. Baek, S.H. Min, O.J. Kwon, W.S. Lee, G.-S. Park. *Int. Journal of Refractory Metals and Hard Materials* **2013**, *38*, 60–66

13. R.L. Axelbaum, J.I. Huertas, C.R. Lottles, S. Hariprasad, and S.M. L. Sastry. *Mater. Manuf. Processes* **1996**, *11*, 1043.

14. P.K. Sahoo, S.S.K. Kamal, M. Premkumar, T. Jagadeesh Kumar, B. Sreedhar, A.K. Singh, S.K. Srivastava, and K. Chandra Sekhar. *Int. J. Refract. Met. Hard. Mater.* **2009**, *27*, 784.

15. Y. Gao, J. Zhao, Y. Zhu, S. Ma, X. Su, and Z. Wang. *Mater. Lett.* **2006**, *60*, 3903.

16. N.J. Welham. *J. Mater. Res.* **1999**, *14*, 619.

17.Z. J. Wu, *Chem. Phys. Lett.* **2003**, *370,* 510.

18. H. Weidele, D. Kreisle, E. Recknagel, et al.. *Chem. Phys. Lett.* **1995**, *237*, 425.

19.X. R. Zhang, X. L. Ding, B. Dai, and J. L. Yang. *J. Mol. Struct.: THEOCHEM* **2005**, *757*, 113.

20. H. Weidele, D. Kreisle, E. Recknagel, G. Schulze Icking-Konert, H. Handschuh, G. Ganteför, and W. Eberhardt. *Chem. Phys. Lett.* **1995**, *237*, 425.

21.X. Zhamg. *Journal of Molecular Structure : THEOCHEM* **2008**, *867*,17-21.

22.X. Zhang, X. Ding, J. Yang. *Int. J. Mod. Phys. B* **2005**, *19*, 2427.

23. H. Weidele, D. Kreisle, E. Recknagel, G.S. Icking-Konert, H. Handschuh, G.Ganteför, W. Eberhardt. *Chem. Phys. Lett.* **1995**, *237* 425.

24. D.T. Birtwistle, A. Herzenberg. *J. Phys. B.* **1971**, *4*, 53.

25. T. Trickl, E.F. Cromwell, Y.T. Lee, A.H. Kung. *J. Chem. Phys*. **1989**, *9*1, 600.

26.W. Yamaguchi and J. Murakami. *Chem. Phys.* **2005**, *316*, 45.

27. K. A. Jackson, M. Horoi, I. Chaudhuri, T. Frauenheim, and A. A. Shvartsburg. *Phys Rev Lett* **2004**, *93*, 4.

28. M. L. Yang, K. A. Jackson, C. Koehler, T. Frauenheim, and J. Jellinek. *J Chem Phys* **2006**, *124*, 024308.

29. D. J. Wales and J. P. K. Doye. *J Phys Chem A* **199**7,*101*, 5111-5116.
30. D. J. Wales and H. A. *Scheraga, Science* **199**9, *285*, 1368-1372.
31. V. Rosato, M. Guillope, and B. Legrand. *Philos Mag A-Phys Condens Matter Struct Defect Mech Prop* **1989**, *59*, 321-336.
32. F. Cleri and V. Rosato. *Phys Rev B* **1993**, *48*, 22.
33. Finnis M W and Sinclair J E. *Phil. Mag. A* **1984**, *50*,45
34. D. C. Liu and J. Nocedal. *Mathematical programming* **1989**, *45*, 503-528.
35. M. A. Karolewski. *Radiat Eff Defects Solids* **2001**, *153*, 239-255.
36. B. Delley. *J Chem Phys* **1990**, *92*, 508-517.
37. B. Delley. *J Chem Phys* **2000**, *113*, 7756-7764 .
38. D. C. Langreth and J. P. Perdew. *Phys Rev B* **1980**, *21*, 5469-5493.
39. J. P. Perdew, J. A. Chevary, S. H. Vosko, K. A. Jackson, M. R. Pederson, D. J. Singh, and C. Fiolhais. *Phys Rev B* **1992**, *46*, 6671-6687.
40. K. B. J.P. Perdew, M. Ernzerhof. *Phys Rev B* **1996**, *77*, 3865.
41.J. D. Honeycutt and H. C. Andersen. *Journal of Physical Chemistry,* **1987**, *91*, 4950-4963.
42. H. J. F. Jansen and A. J. Freeman. *Phys. Rev. B* **1984**, *30*, 561
43. J. W. Davenport, M. Weinert, and R. E. Watson. *Phys. Rev. B* **1985**, *32*, 4876
44. Jiguang Du, Xiyuan Sun, Daqiao Meng, Pengcheng Zhang, and Gang Jiang. *J. Chem. Phys.* **2009**, *131*, 044313.
45. Michael J. Mehl and Dimitrios A. Papaconstantopoulos, *Phys. Rev. BP* **1996**, *54*, 4519
46.L.T. Kong, J.B. Liu, W.S. Lal, B.X. Liu. *Journal of Alloys and Compounds* **2002**, *337*, 143–147.
47.Z. Hu, J. G. Dong, J. R. Lombardi, and D. M. Lindsay. *J. Chem. Phys* **1992**,*97*, 8811.
48. 35M. D. Morse, *Chem. Rev.* (Washington, D.C.) **1986**, *86*, 1049.
49. P. Villars, L. D. Calvert, and W. B. Pearson. *Acta Crystallogr Sect A* **1984**, *40*, C444-C444.
50. M. X. Chen and X. H. Yan. *J Chem Phys* **2008**, *128*, 174305.
51. M. S. Lee, S. Chacko, and D. G. Kanhere. *J Chem Phys* **2005**, *123*,164310.
52. S. M. Ghazi, M. S. Lee, and D. G. Kanhere. *J Chem Phys* **2008,** *128*, 104701.
53.W. Fa and J. M. Dong, *J Chem Phys* **2006** *124*,114310.
54. F. Chen and R. L. Johnston. *Acta Mater* **2008**, *56*, 2374-2380.
55. P. K. Jain. *Struct Chem* **2005**,*16*, 421-426.

Address of the corresponding author:
Author: Shin-Pon Ju
Institute: Department of Mechanical and Electro-Mechanical Engineering,
National Sun Yat-Sen University
Street: 70 Lienhai Rd.
City: Kaohsiung
Country: Taiwan
Telephone: +886-7-5252633~34 4268
Fax:+886-7-5252630
Email: jushin-pon@mail.nsysu.edu.tw

Table 1 Parameters used in the bulk tight-binding potential.

Parameters	**A(eV)**	**ζ(eV)**	**p**	**q**	**r_0** (Å)
W_{bulk}	0.249	3.2055	10.3715	1.9916	2.741

Table 2 The results of binding energy using BPW91and PW91 functional for bulk tungsten materials

		EXP	***PW91/DNP/DSPP***	***BPW91/DNP/DSPP***
W_{FCC}	Cohesive Energy	8.33~8.45[a]	8.36	
W_{HCP}	Cohesive Energy	8.33[b]	8.19	
W_{BCC}	Cohesive Energy	8.9[a]	8.9	8.674
	Lattice constant	3.16[c] 3.25[d]	3.165	3.165

[a]Reference 42, [b]Reference 43, [c]Reference 45, [d]Reference 46

Table 3 The results of bonding, frequency, and dissociative energy using BPW91and PW91 functional for tungsten dimer

	Method	**R (Å)**	**ω(cm^{-1})**	**E_d(eV)**
W_2	PW91/DNP/DSPP	2.05[h]	310.5[h]	5.44[h]
	BPW91/DNP/DSPP	2.053[e]	376[e]	5.22[e]
	Expt.		337[f]	5 ±1[g]

[e]Reference 44, [f]Reference 47, [g]Reference 48, [h]This work

Table 4 The average binding energy of W_n (n=2-16) ground-state geometries by the sets of PW91/DNP/DSPP and BPW91/DNP/DSPP

Cluster	R_{av}(Å)	Eb/atom(eV)	
		BP	PW91
W_2	2.051	2.65	2.67
W_3	2.324	3.60	3.70
W_4	2.404	4.07	4.19
W_5	2.467	4.57	4.70
W_6	2.479	4.88	5.02
W_7	2.508	5.08	5.22
W_8	2.510	5.29	5.41
W_9	2.530	5.38	5.52
W_{10}	2.541	5.45	5.61
W_{11}	2.545	5.57	5.73
W_{12}	2.563	5.62	5.78
W_{13}	2.561	5.70	5.84
W_{14}	2.580	5.75	5.90
W_{15}	2.583	5.79	5.96
W_{16}	2.590	5.85	6.03

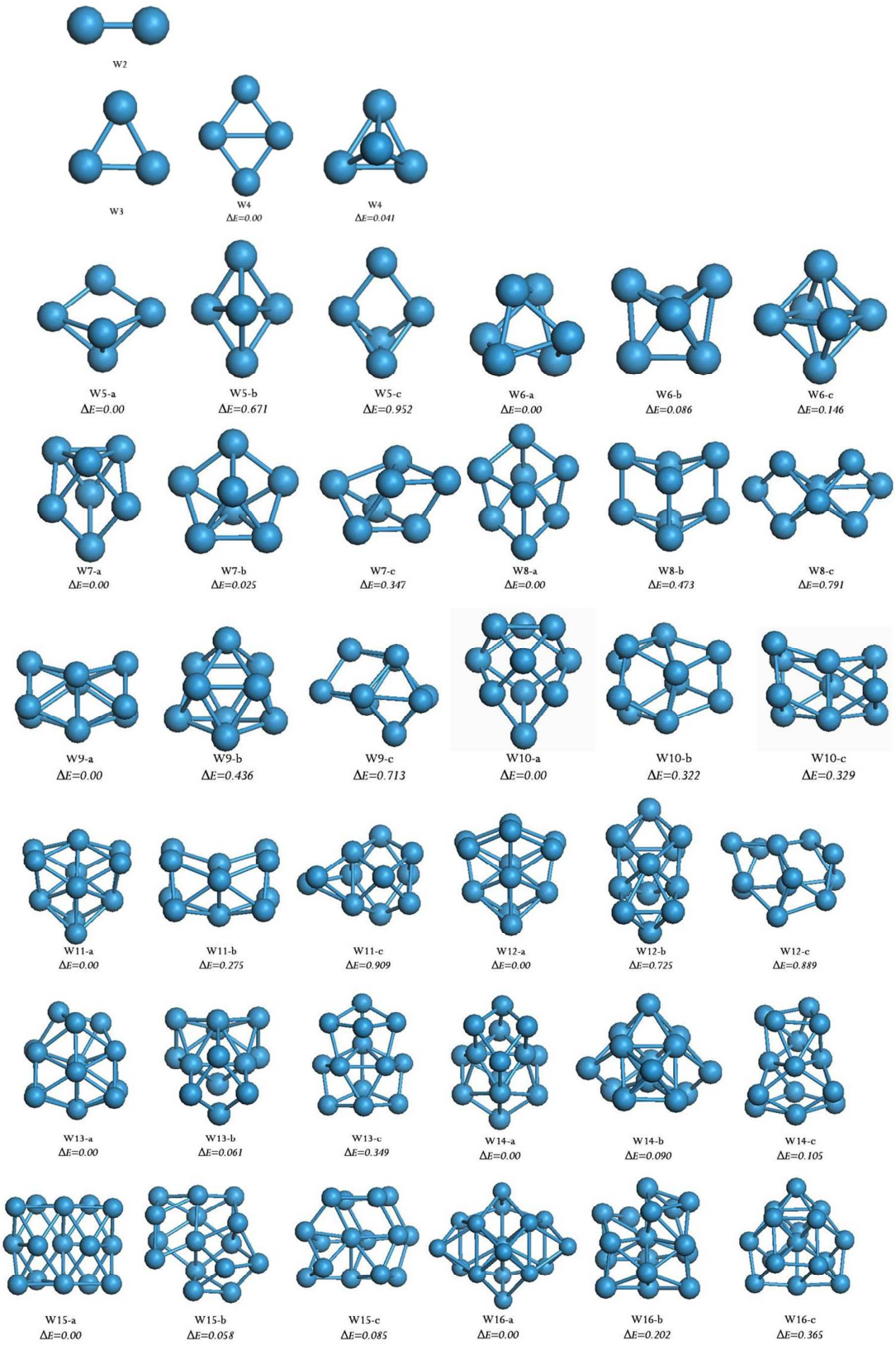

Figure 1 W_n (n=2-16) ground-state geometries with isomer structures and energies relative to the energies of their ground states. The unit of energy is eV.

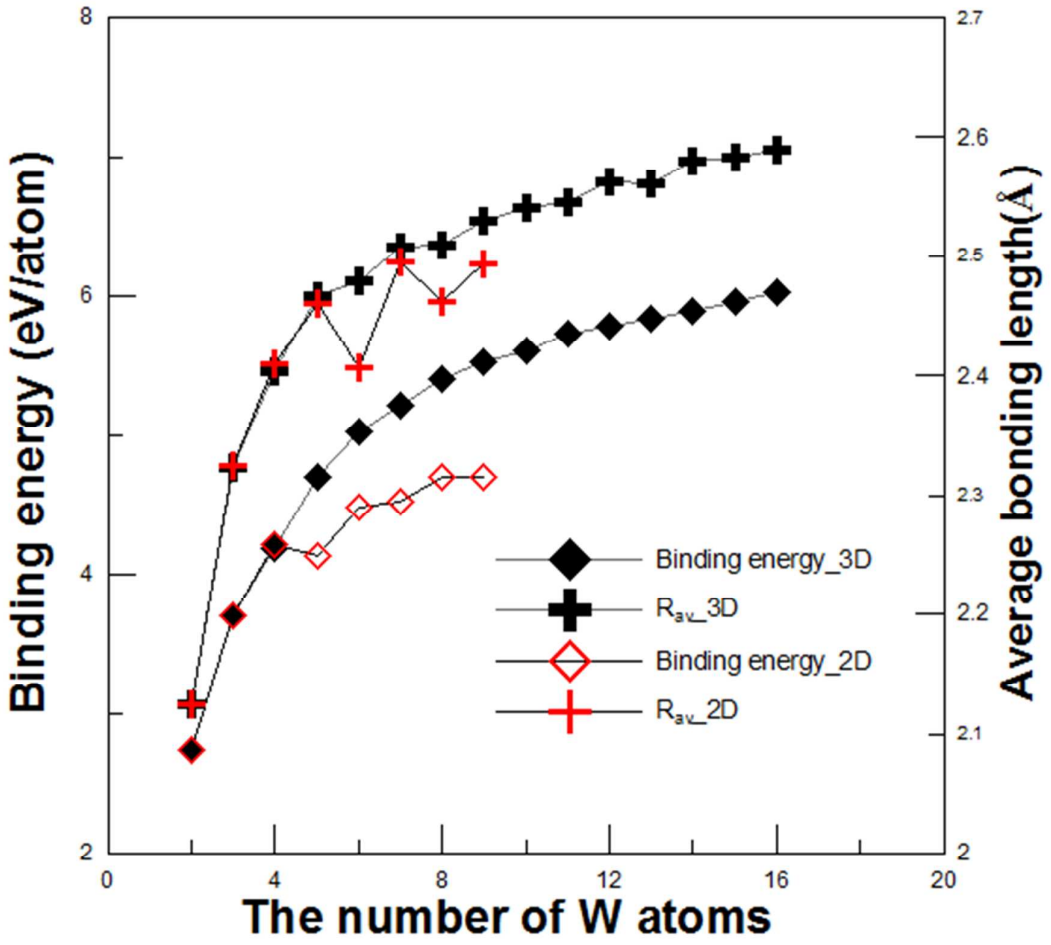

Figure 2 The binding energy (eV) and average bond length of the 2D and 3D ground-state structures as a function of number of W atoms.

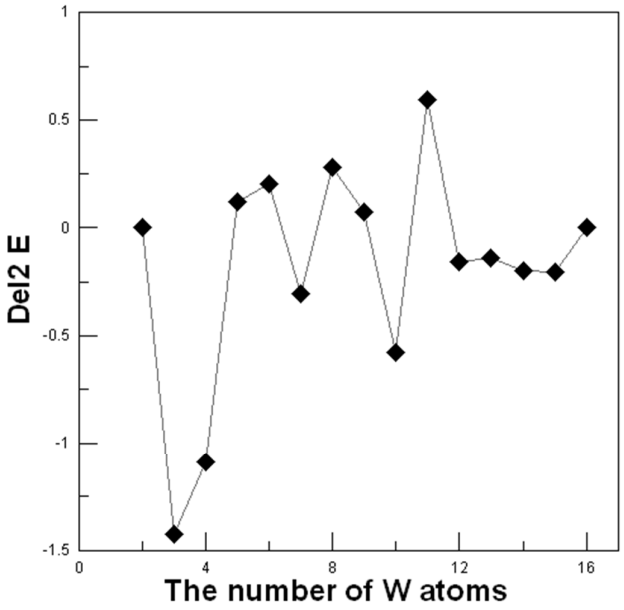

Figure 3 The plot of Δ_2E for different number of W atoms.

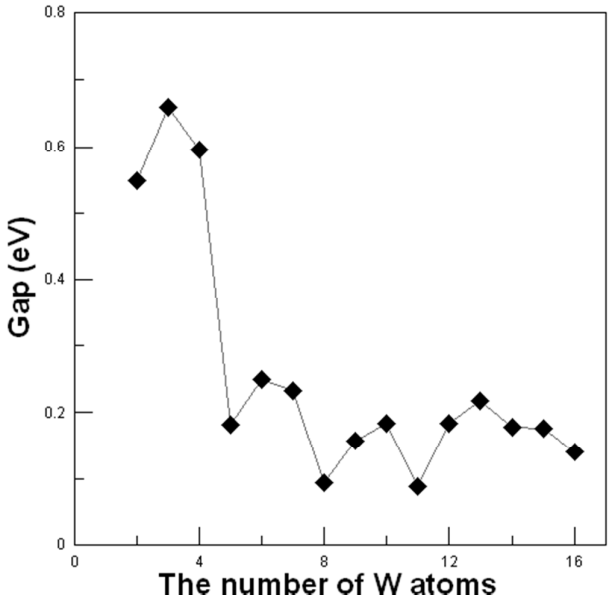

Figure 4 The plot of HOMO-LUMO gaps for different number of W atoms.

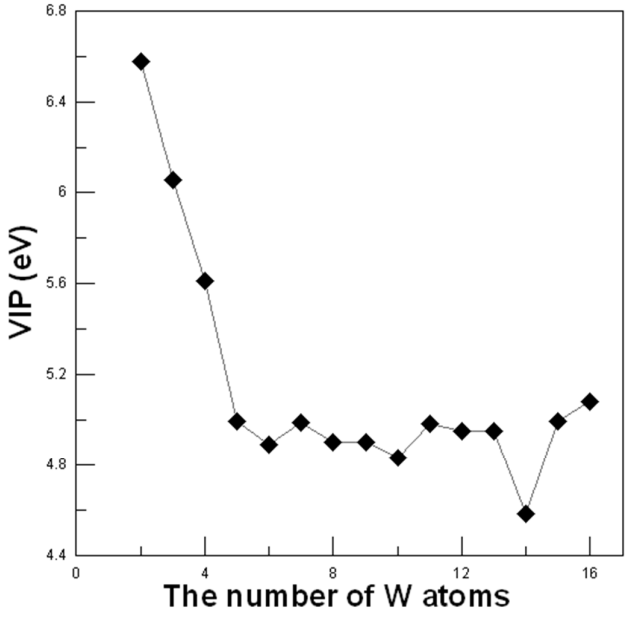

Figure 5 The vertical ionization potential (VIP) shown as a function of number of W atoms

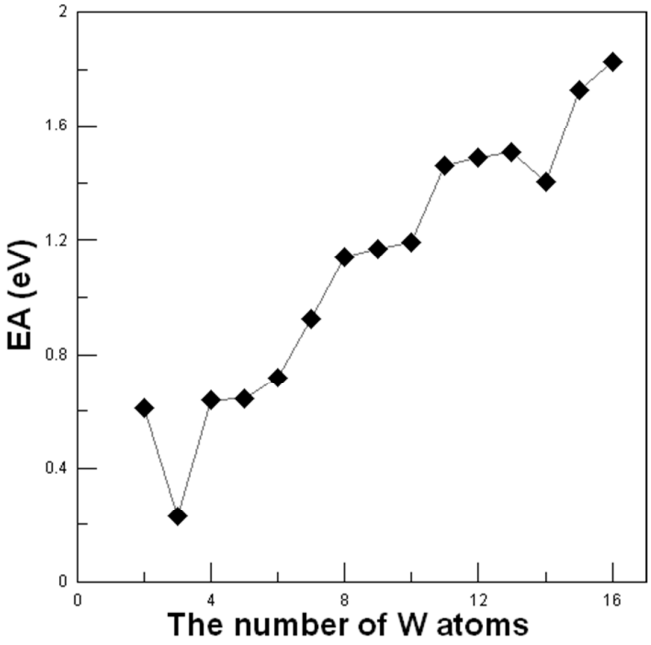

Figure 6 The adiabatic electron affinities (AEAs) shown as a function of number of W atoms

Table 5 The W_n (n=2-16) nanocluster charges for*5d*, *6s*, and *6p* orbitals by population analysis

Atom	Orbit	Charge	Sum
W_2	5d	4.901	6.008
	6s	1.503	
	6p	0.054	
W_3	5d	4.561	6.002
	6s	1.264	
	6p	0.177	
W_4	5d	4.442	6.0
	6s	1.362	
	6p	0.197	
W_5	5d	4.533	5.995
	6s	1.237	
	6p	0.226	
W_6	5d	4.539	5.994
	6s	1.212	
	6p	0.244	
W_7	5d	4.478	5.992
	6s	1.215	
	6p	0.298	
W_8	5d	4.497	5.99
	6s	1.226	
	6p	0.268	
W_9	5d	4.471	5.99
	6s	1.201	
	6p	0.317	
W_{10}	5d	4.521	5.988
	6s	1.186	
	6p	0.280	
W_{11}	5d	4.499	5.987
	6s	1.189	
	6p	0.30	
W_{12}	5d	4.483	5.987
	6s	1.193	
	6p	0.311	
W_{13}	5d	4.488	5.986
	6s	1.188	
	6p	0.311	
W_{14}	5d	4.498	5.988
	6s	1.2	
	6p	0.29	
W_{15}	5d	4.479	5.986
	6s	1.178	
	6p	0.329	
W_{16}	5d	4.464	5.985
	6s	1.184	
	6p	0.337	

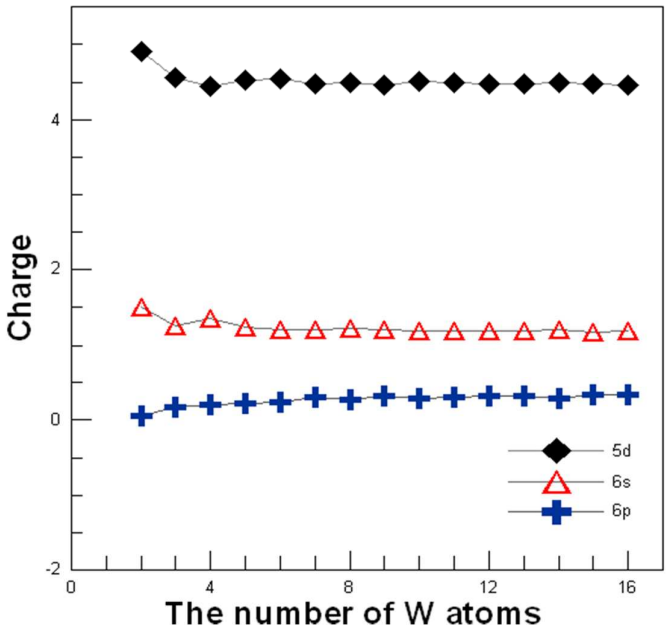

Figure 7 The charge distribution for 5d, 6s, and 6p orbitals

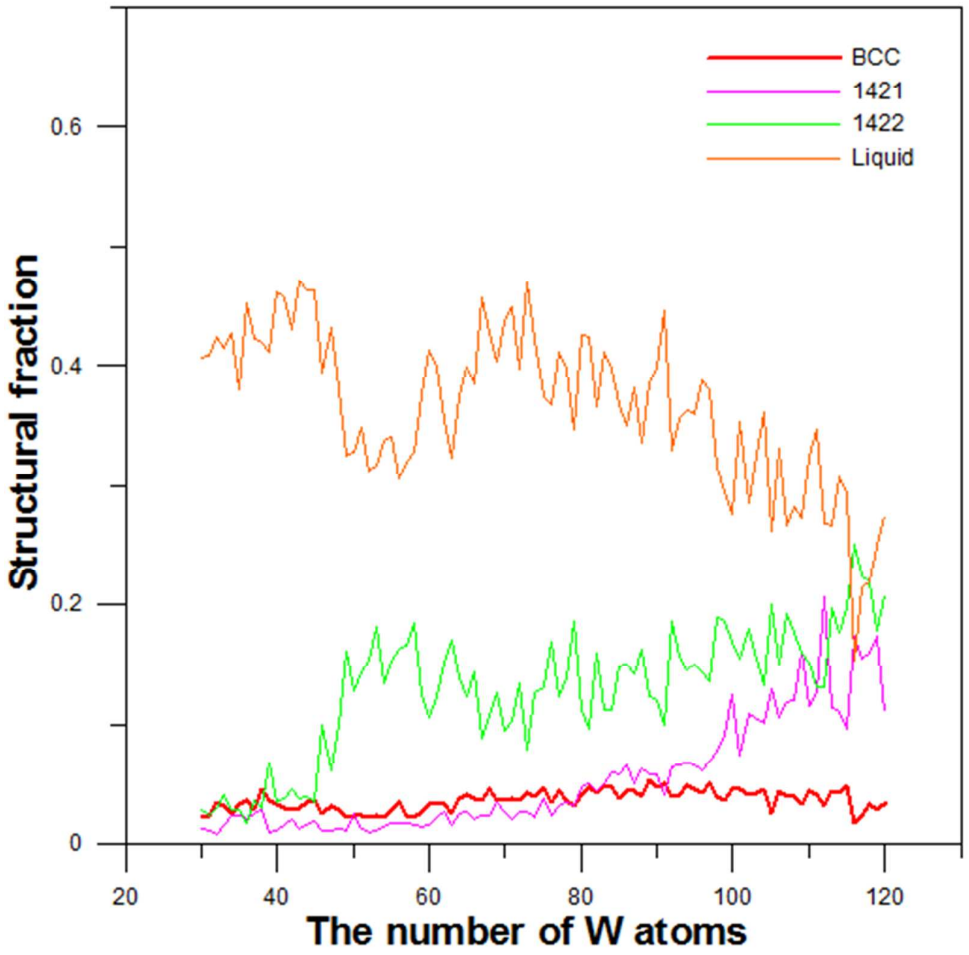

Figure 8 The distribution of structures found using TB potential for large size nanoclusters W_n (n=30-120). The red, pink, green, and orange lines are the fractions of BCC, FCC, FCC-HCP phase, and amorphous structures, respectively.

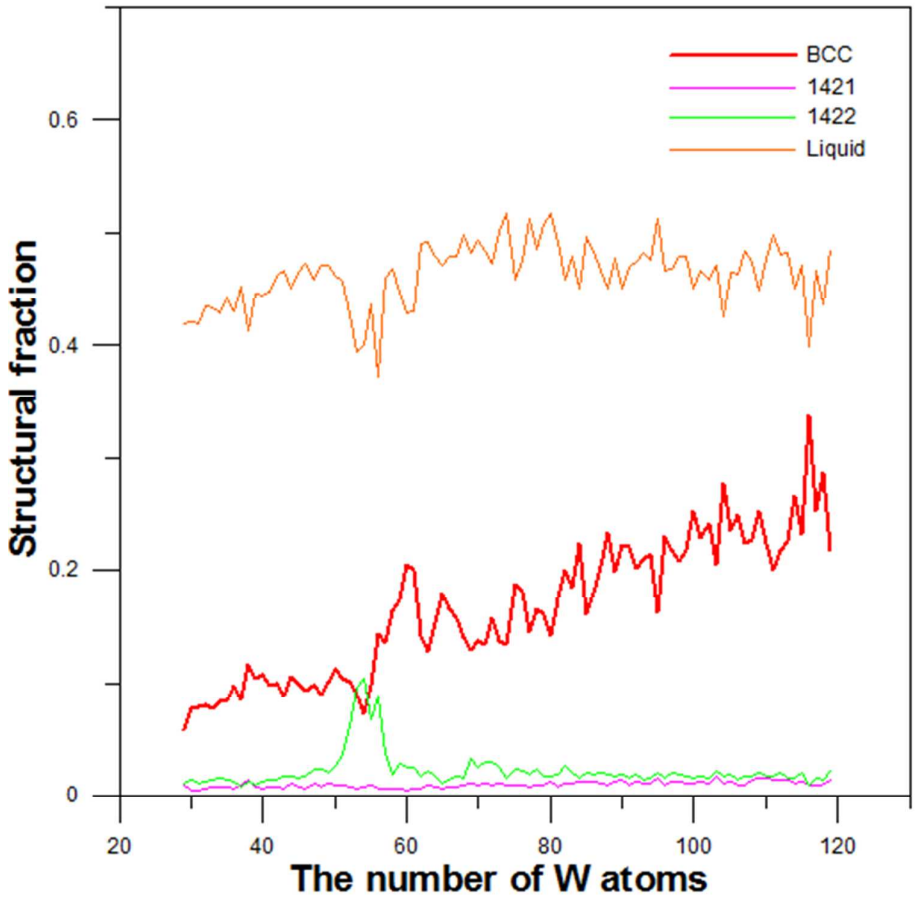

Figure 9 The distribution of structures found using FS potential for large size nanoclusters W_n (n=30-120). The red, pink, green, and orange lines are the fractions of BCC, FCC, FCC-HCP phase, and amorphous structures, respectively.

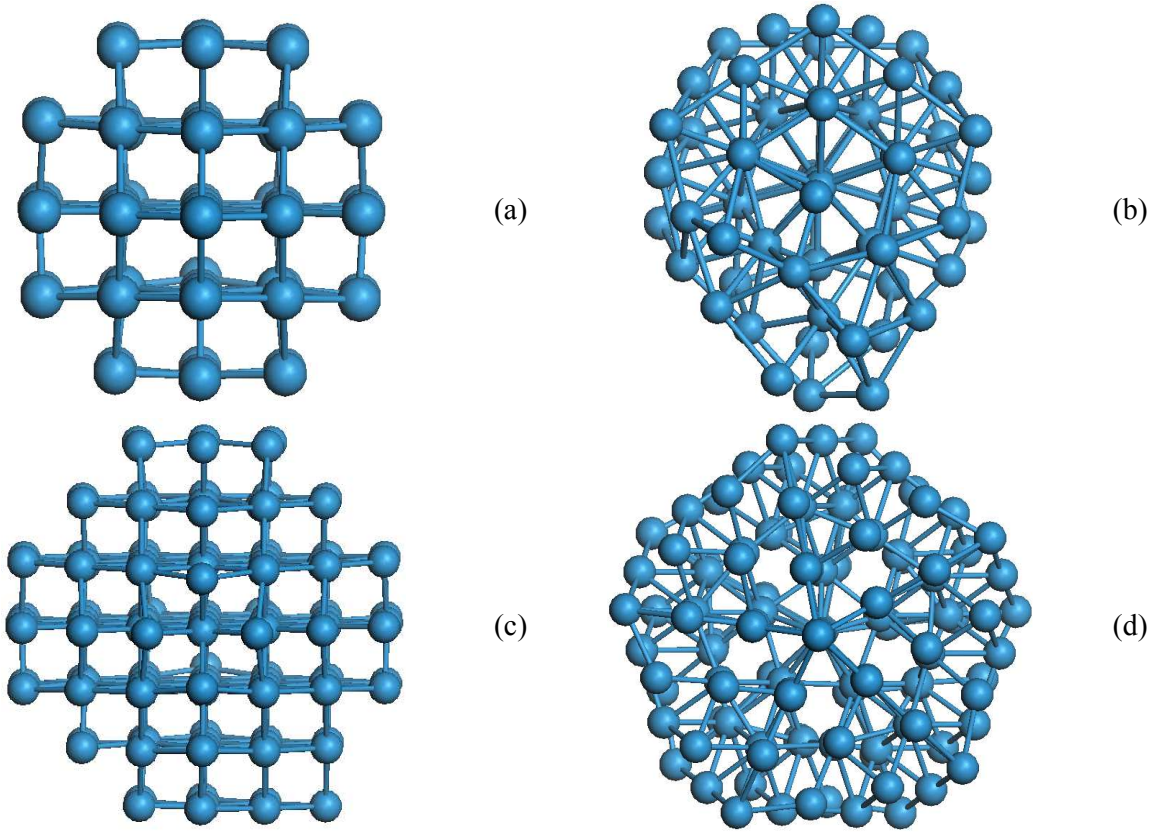

Figure 10 W_{60} found by BH method with (a)FS and (b) TB potentials; W_{116} structures calculated by BH method with(c) FS and (b) TB potentials.

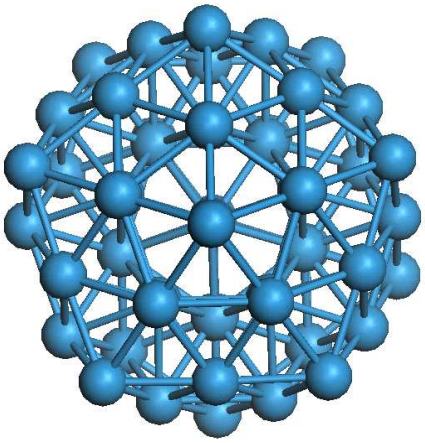

(a)

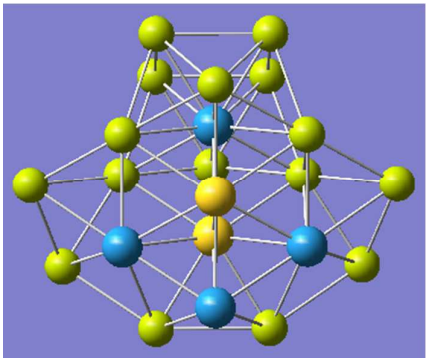

(b)

Figure 11 (a) W_{54} found by both FS and TB potential methods; (b) the partial structure of the W_{54} nanoclusters